SUPPLEMENTARY ONLINE MATERIAL

An Electrochemically Active Textile Current Collector with a High Areal Capacity and a Strong Energy Recovery Effect Using an Interfacial Interaction Assembly

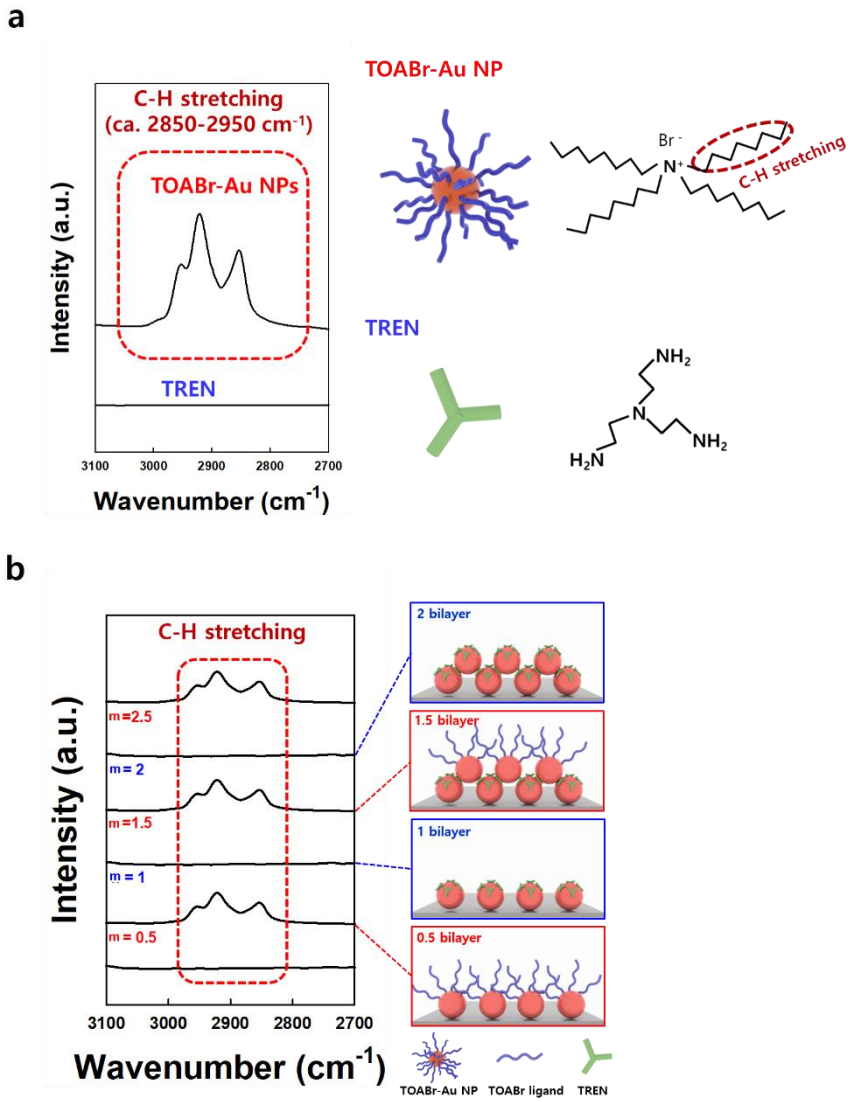

Fig. S1. (a) FTIR spectra of TOABr-Au NP and TREN (left) and representative molecular structures of TOABr ligand and TREN (right). In this case, only TOABr-Au NP displayed characteristic peaks at 2850-2950 cm^{-1} for C-H stretching vibration originating from long alkyl chains of TOABr ligands. (b) FTIR spectra and their corresponding scheme images of LbL-assembled (TOABr-Au NPs/TREN)$_m$ multilayers as a function of the bilayer number (m). The characteristic peaks for C-H stretching mode originating from TOABr ligands alternatively appeared and disappeared depending on the outermost layer of the multilayers during LbL assembly, clearly indicating that native TOABr ligands bound to the Au NP surface were completely replaced by the amine moieties of TREN.

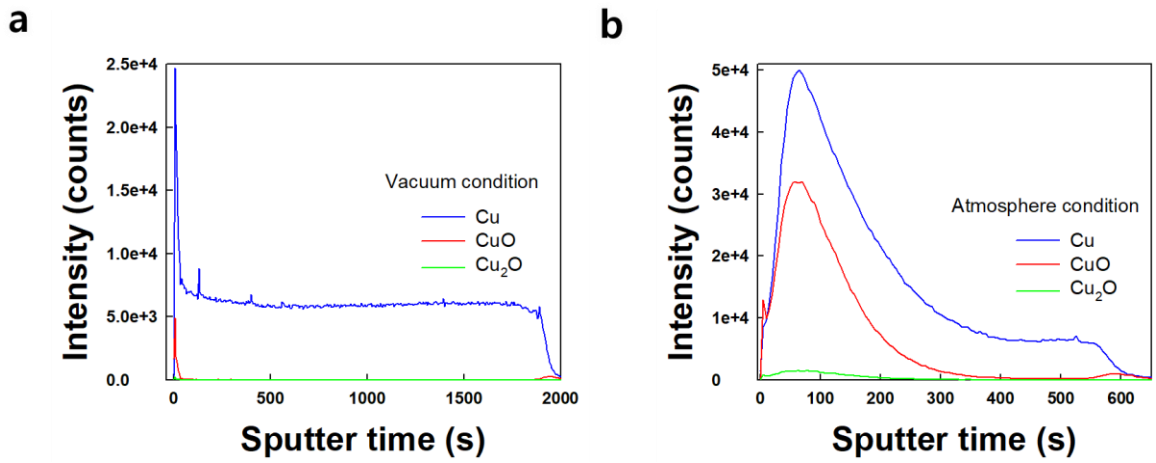

Fig. S2. TOF-SIMS profiles of Cu-electroplated/Au-sputtered Si wafer (i.e., EP Cu-Au/Si wafer) prepared from thermal annealing under (a) vacuum and (b) atmosphere conditions. These results suggest that the outermost copper oxide can be formed through an adequate annealing under atmosphere condition. The signals for CuO and Cu_2O were observed clearly at the beginning of beam sputtering, and then gradually attenuated up to 400 s, whereas the signal for the Cu metal layer was maintained for sputtering time of 600 s. These results indicate that the mixed layer of Cu, CuO, and Cu_2O (composition ratio: Cu > CuO > Cu_2O) was formed onto Cu metal layer with thickness of ~125 nm. In this case, the thickness of Cu metal layer was calculated from the beam sputter time and TOF-SIMS data of oxide-removed EP Cu-Au/Si wafer.[S1] The EP Cu-Au/Si wafer was prepared by electroplated Cu layer with the thickness of ~1 μm.

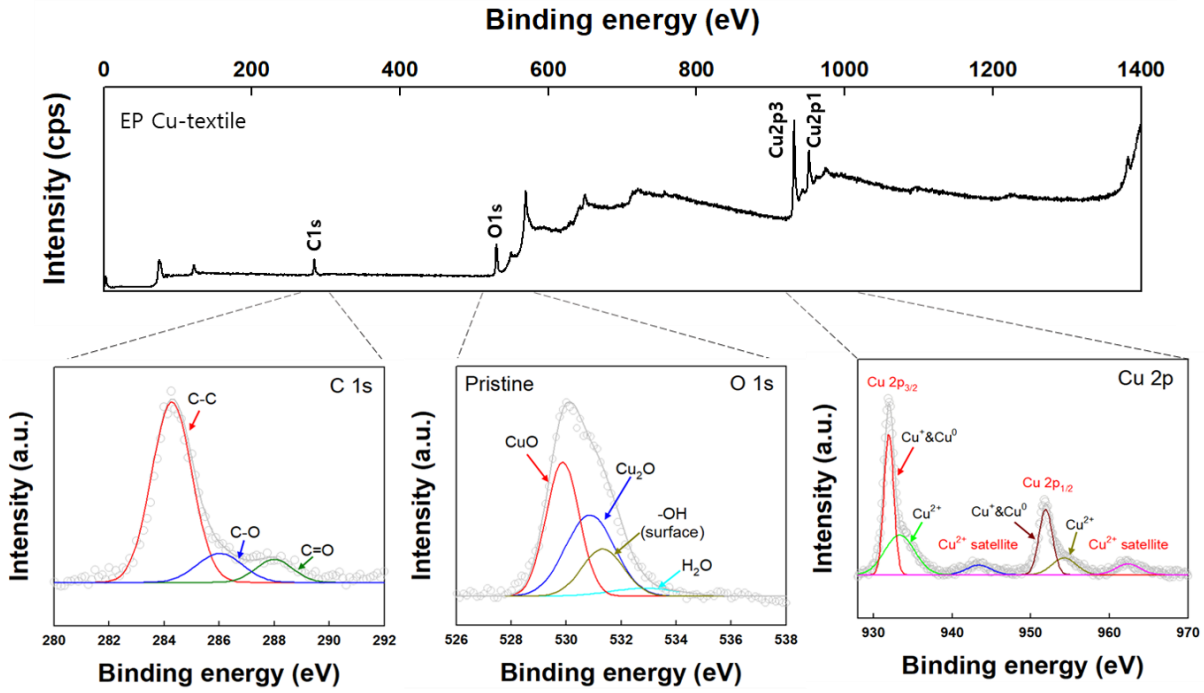

Fig. S3. Wide-survey XPS spectra of EP Cu-textile (top) and deconvoluted spectra for C 1s, O 1s, and Cu 2p core levels (bottom). The O 1s spectrum was deconvoluted into four components by Gaussian fitting observed at 529.8, 530.8, 531.6, and 533 eV, corresponding to lattice oxygen of copper oxide (i.e., Cu_2O and CuO), chemisorbed hydroxides, and H_2O on the surface of the EP Cu-textile electrode, respectively.[S2]

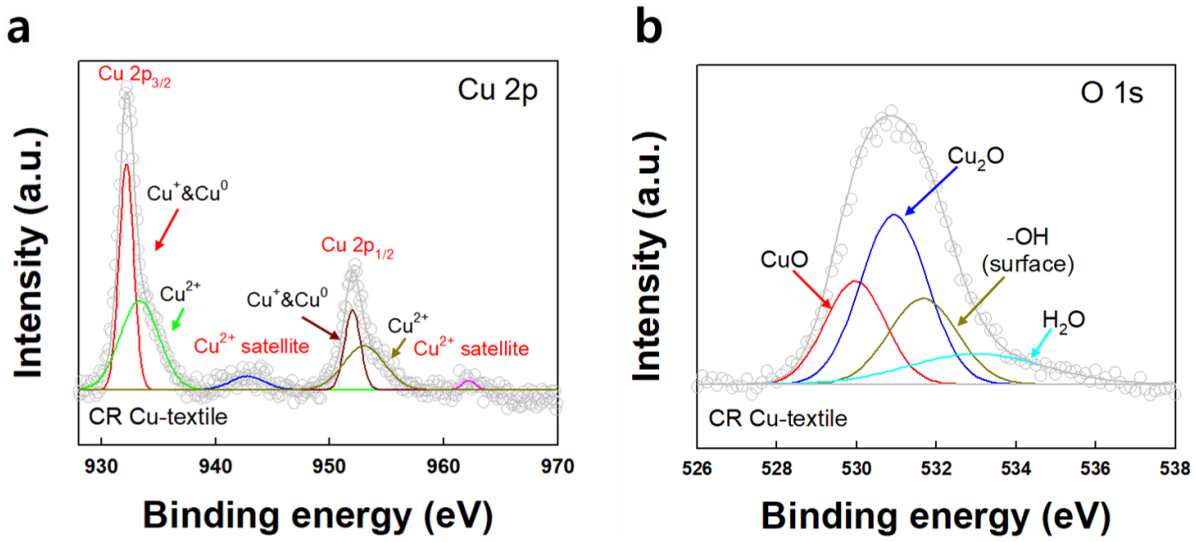

Fig. S4. (a) Cu 2p and (b) O 1s XPS spectra of CR Cu-textile. In this case, the deconvoluted O 1s spectrum imply that the CR Cu-textile contained more Cu_2O than CuO (Fig. S4b). This result may be attributed to a relatively low reduction quality of CR Cu-textile compared to EP Cu-textile. That is, given that the annealing process in our study was carried out at a relatively low temperature, the residual impurities (e.g., reduction agent) remaining within the CR Cu-textile can impede the efficient copper oxidation kinetics, resulting in a higher content of unstable Cu_2O than CuO within the CR Cu-textile.[S3]

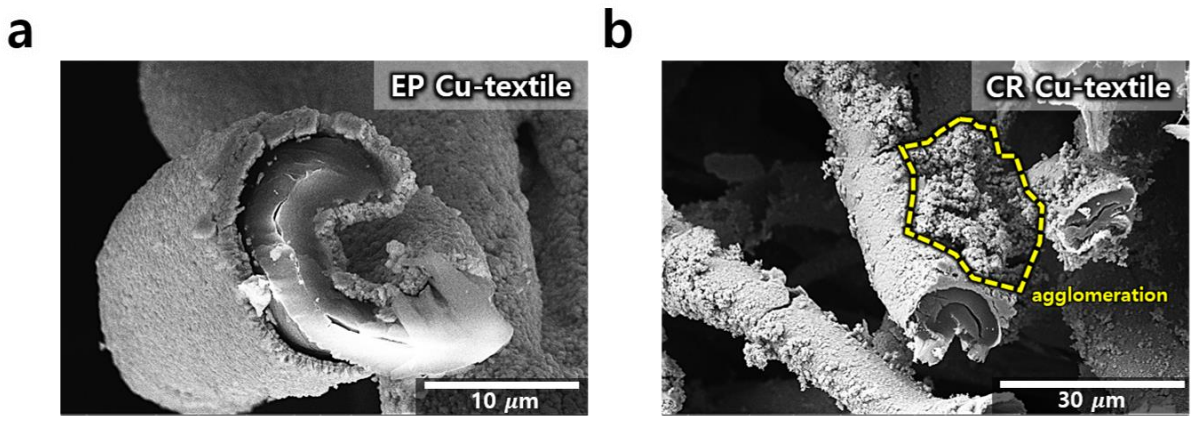

Fig. S5. Cross-sectional FE-SEM images of (a) EP Cu-textile (scale bar, 10 μm) and (b) CR Cu-textile (scale bar, 30 μm). In this case, EP Cu-textile showed the formation of uniform Cu layer, whereas CR Cu-textile displayed poor coating quality showing partial agglomeration.

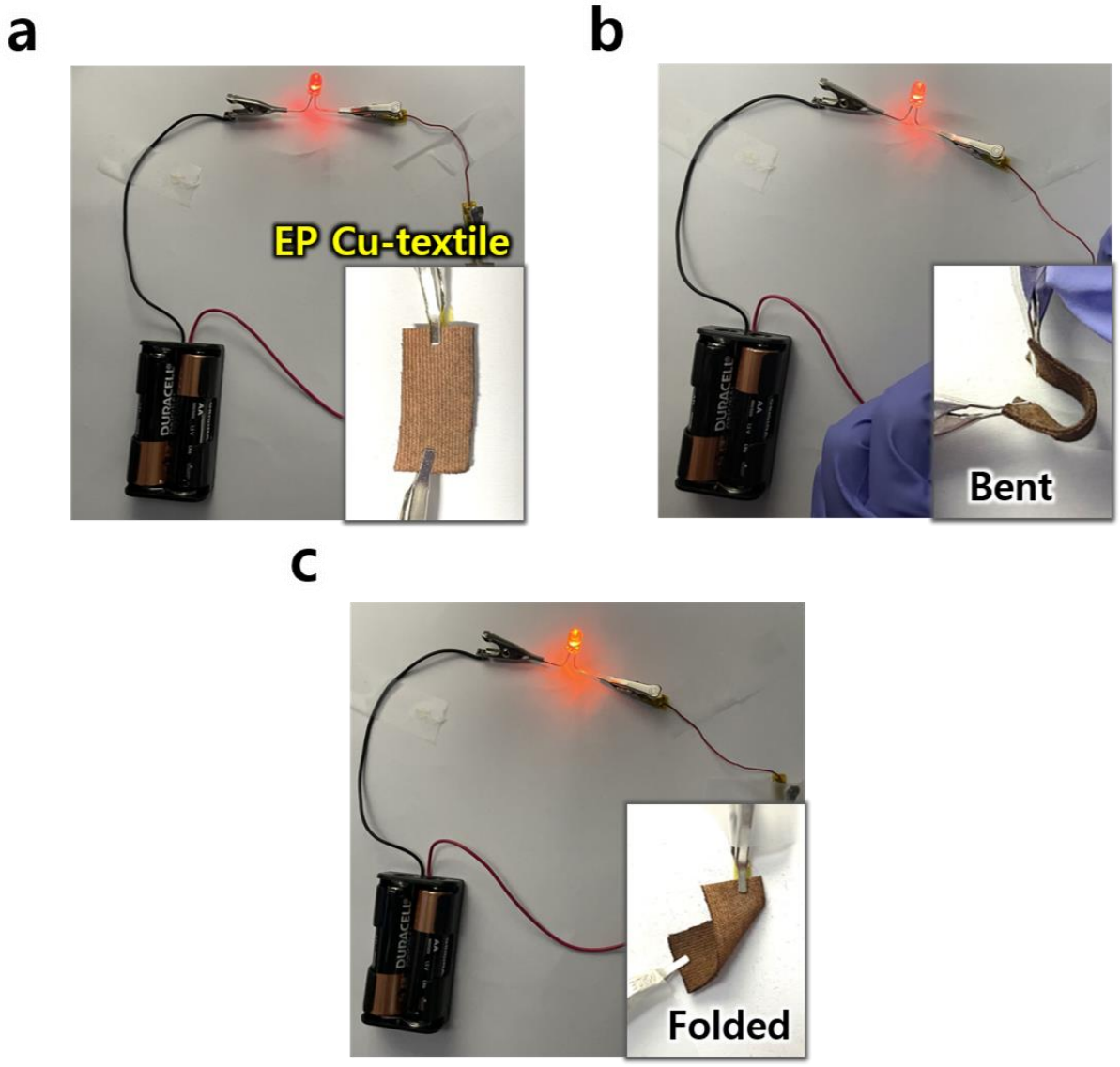

Fig. S6. Photographic images of EP Cu-textile with LED connection under (a) flat, (b) bent, and (c) folded states.

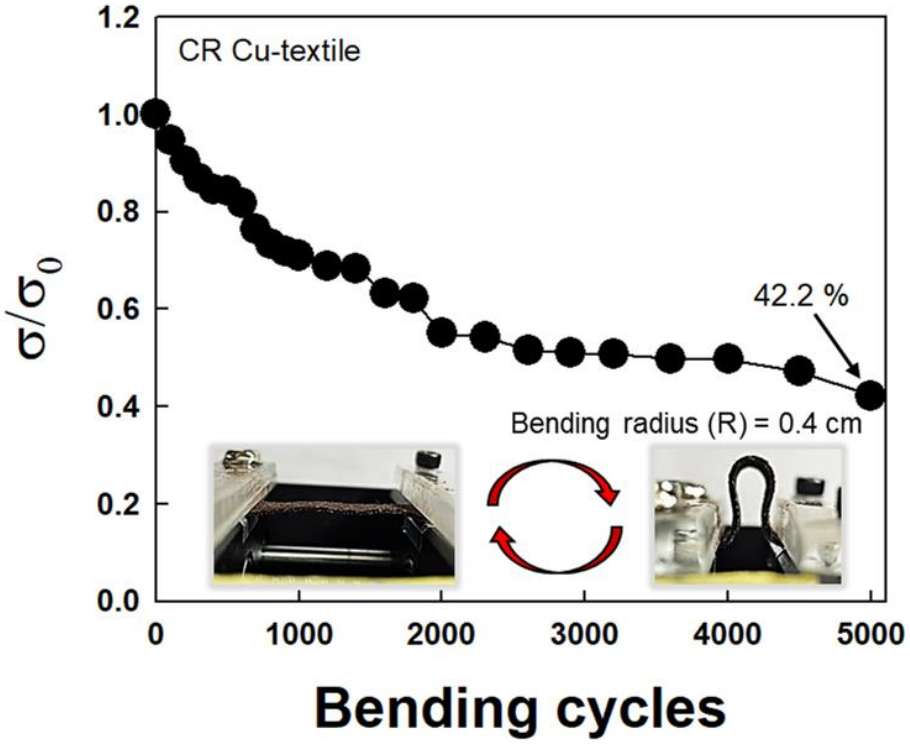

Fig. S7. Electrical stability of CR Cu-textile as a function of the bending cycle number (Bending radius ~ 0.4 cm).

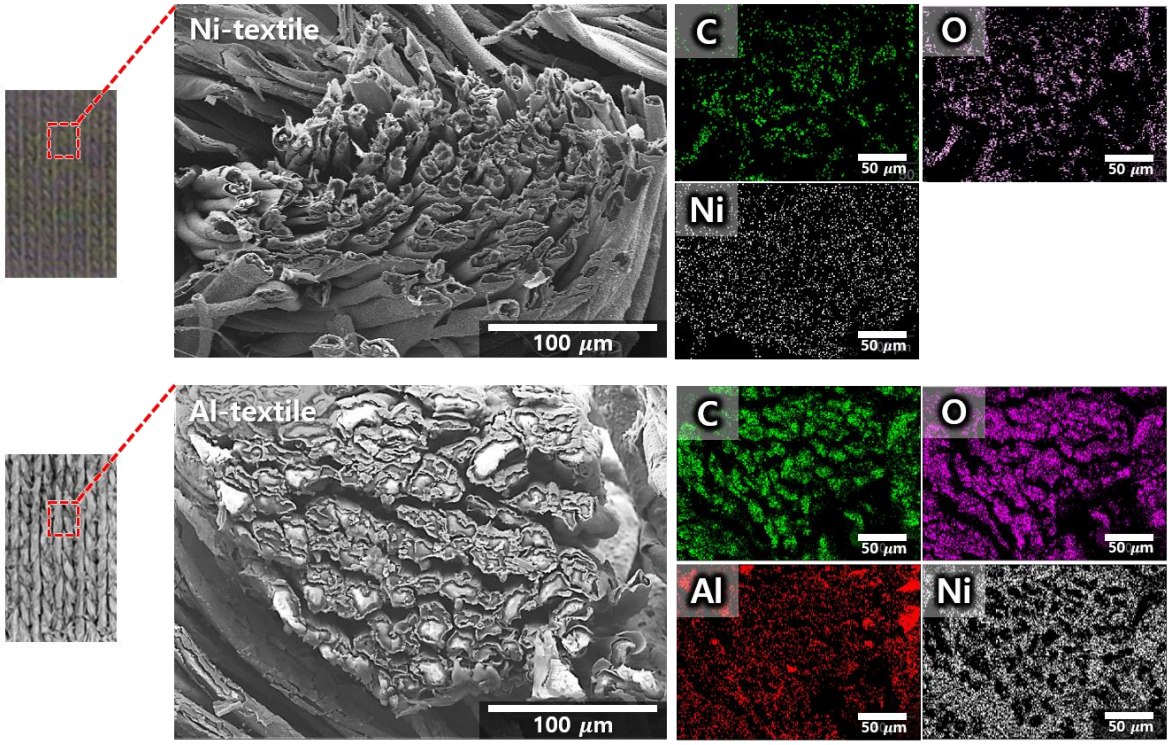

Fig. S8. Cross-sectional FE-SEM images of EP Ni-textile (scale bar, 100 μm) and EP Al-textile (scale bar, 100 μm).

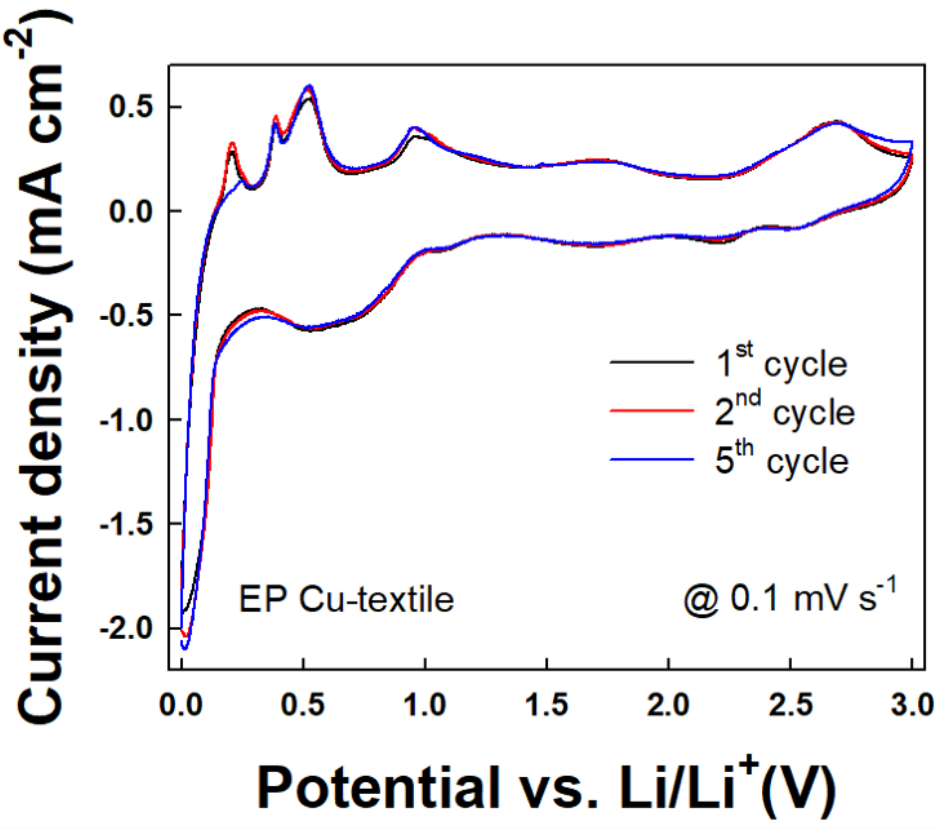

Fig. S9. CV curves of EP Cu-textile in potential window of 0.01 – 3.0 V (vs. Li/Li^+) at a scan rate of 0.1 mV s^{-1}. In this case, the reduction peaks at approximately 2.17, 1.63, and 0.61 V correspond to the formation of $Cu_{1-x}^{II}Cu_x^{I}O_{1-x/2}$ ($0 \leq x \leq 0.4$), Cu_2O (from CuO), and Cu/Li_2O (from Cu_2O), respectively. Additionally, the oxidation peaks at 1.01, 1.17, and 2.75 V were related to the decomposition of the organic layer (Li_2O) and the successive formation of Cu_2O and CuO, respectively.

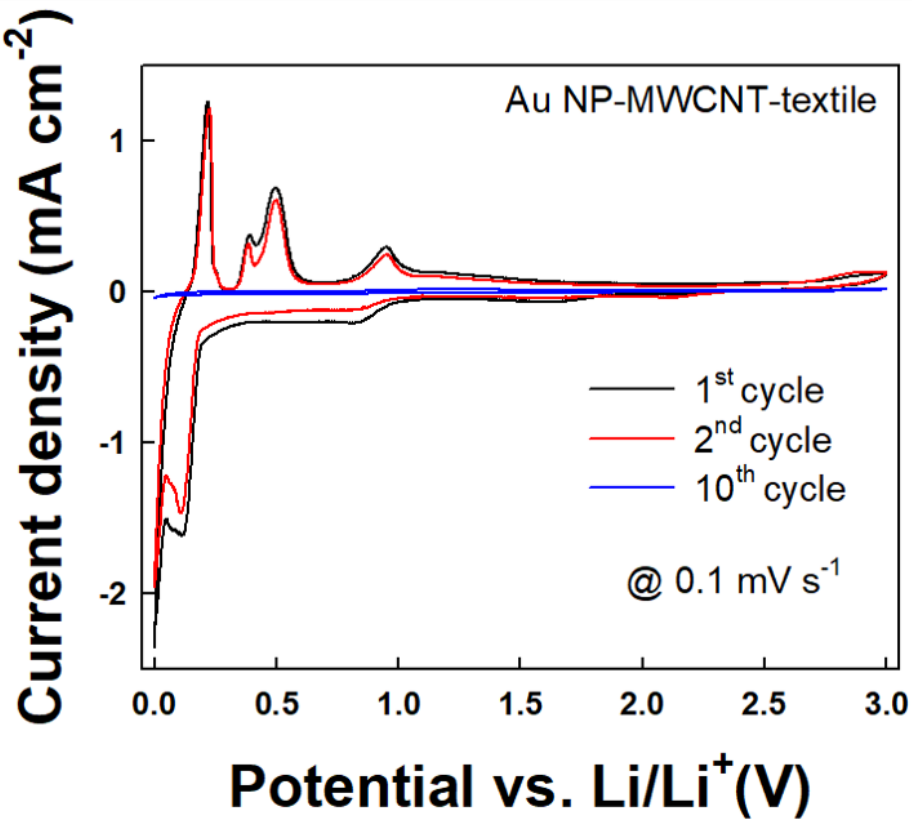

Fig. S10. CV curves of the Au NP-MWCNT-textile at a scan rate of 0.1 mV s^{-1}. All reduction peaks below ~0.2 V vs. Li/Li^+ observed at first and second cathodic sweeps indicate the formation of $Li_{15}Au_4$-intermetallic phases. In the anodic sweeps, the three strong peaks observed at 0.2 V, 0.37 V, and 0.49 V corresponded to the oxidation processes of the Li-intermetallic phase. Additionally, the peak observed at ~0.94 V attributed to the interaction between the lithium ions and surface-oxygenated functional groups (MWCNT).[S4]

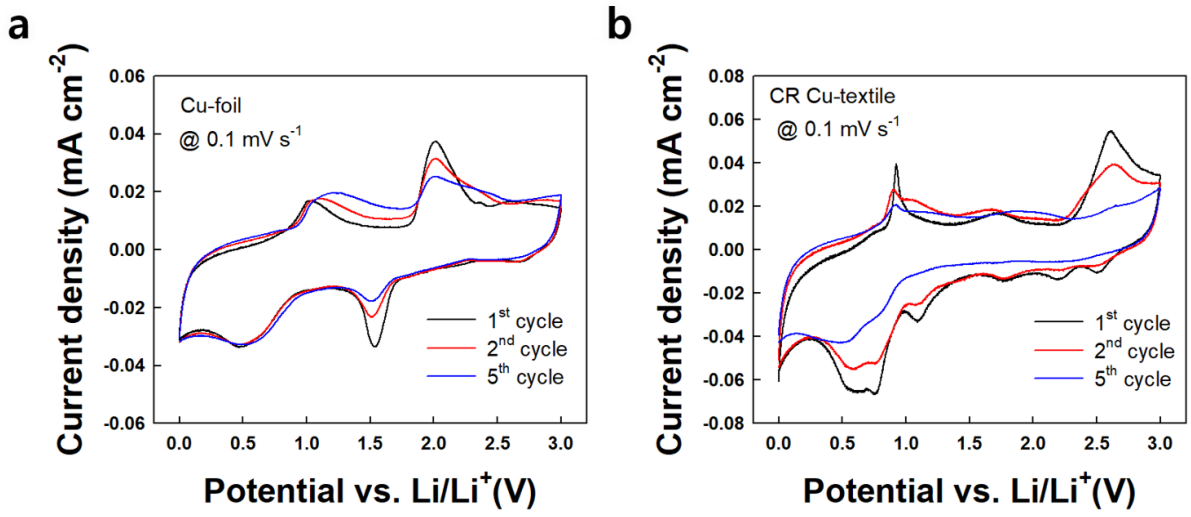

Fig. S11. CV curves of (a) CR Cu-textiles and (b) Cu-foils at a scan rate of 0.1 mV s^{-1}.

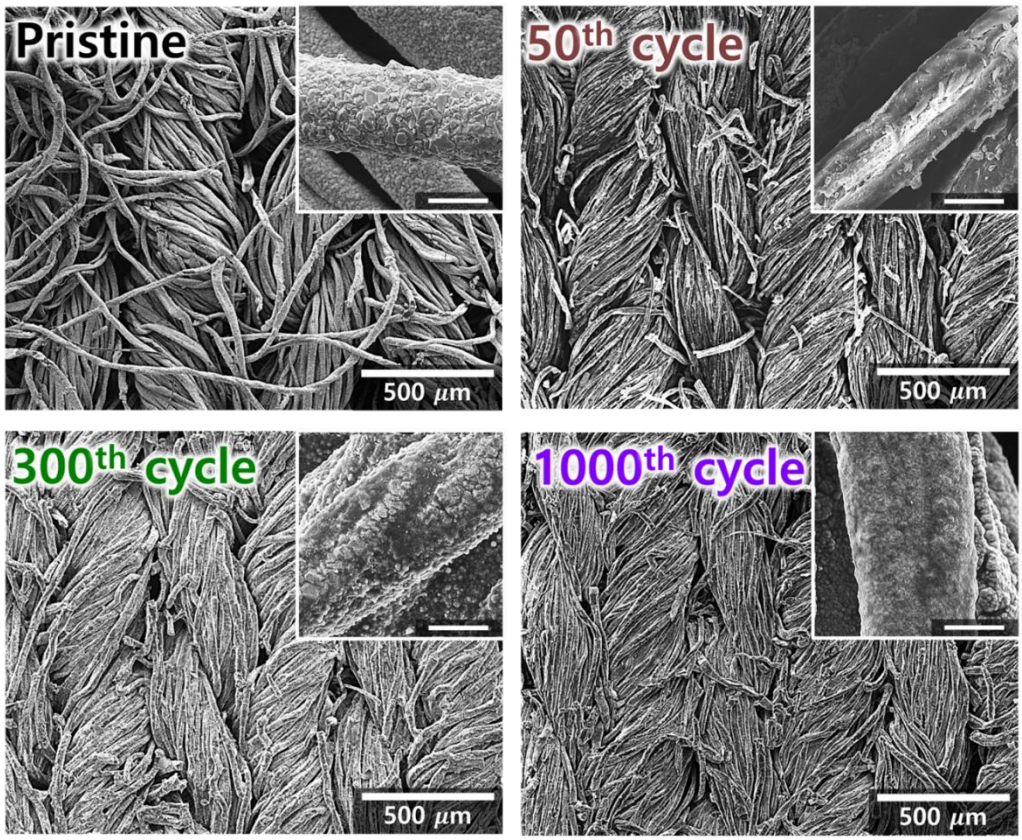

Fig. S12. FE-SEM images of EP Cu-textile at various GCD cycle numbers (scale bar, 10 μm (insets)).

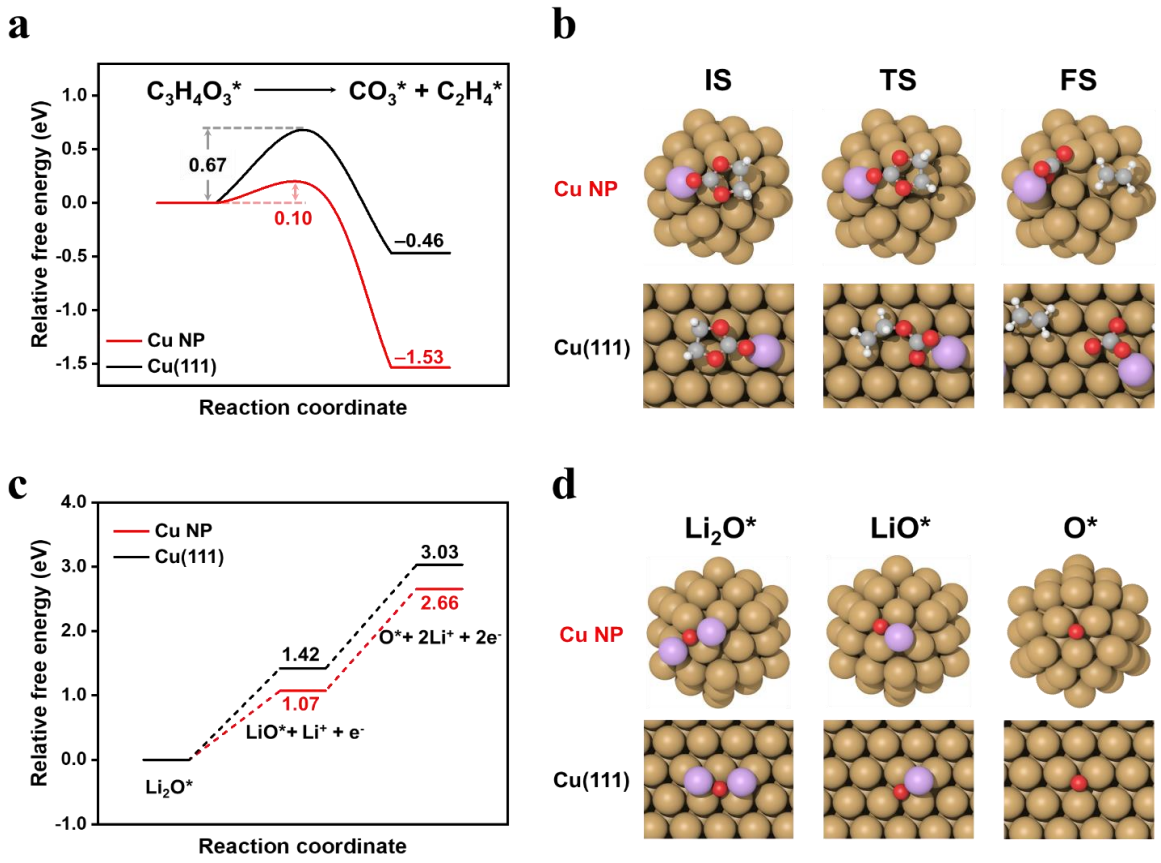

Fig. S13. (a), (b) Activation energy calculation for ethylene carbonate (EC) decomposition on the Cu(111) surface and the Cu NP. The EC decomposition process involved breaking two Ce-Oe bonds of EC and splitting into carbonyl and ethylene. It was found that the EC molecule prefers to adsorb parallel orientation on the Cu (111) surface and the Cu NP. For the configuration of FS, carbonyl was found to be adsorbed parallel to the Cu(111) surface while it adsorbed vertically on the Cu NP. The reaction energies were -0.46 eV for the Cu(111) surface and -1.53 eV for the Cu NP, respectively, indicating that the adsorption of carbonyl and ethylene molecules is energetically more favorable on the Cu NP. Moreover, the activation energies of EC decomposition were found to be 0.67 and 0.10 eV for the Cu(111) surface and the Cu NP, respectively, suggesting that the Cu NP can accelerate the EC decomposition resulting in a facile formation of polymeric gel-like layer. (c), (d) On the other hand, the dissolution behavior of a SEI layer composed of Li_2O was also investigated. DFT results showed that the Cu NP is more beneficial to the decomposition of Li_2O. Here, the free energy of a Li^+-e^- pair is defined that of Li metal at 0 V.

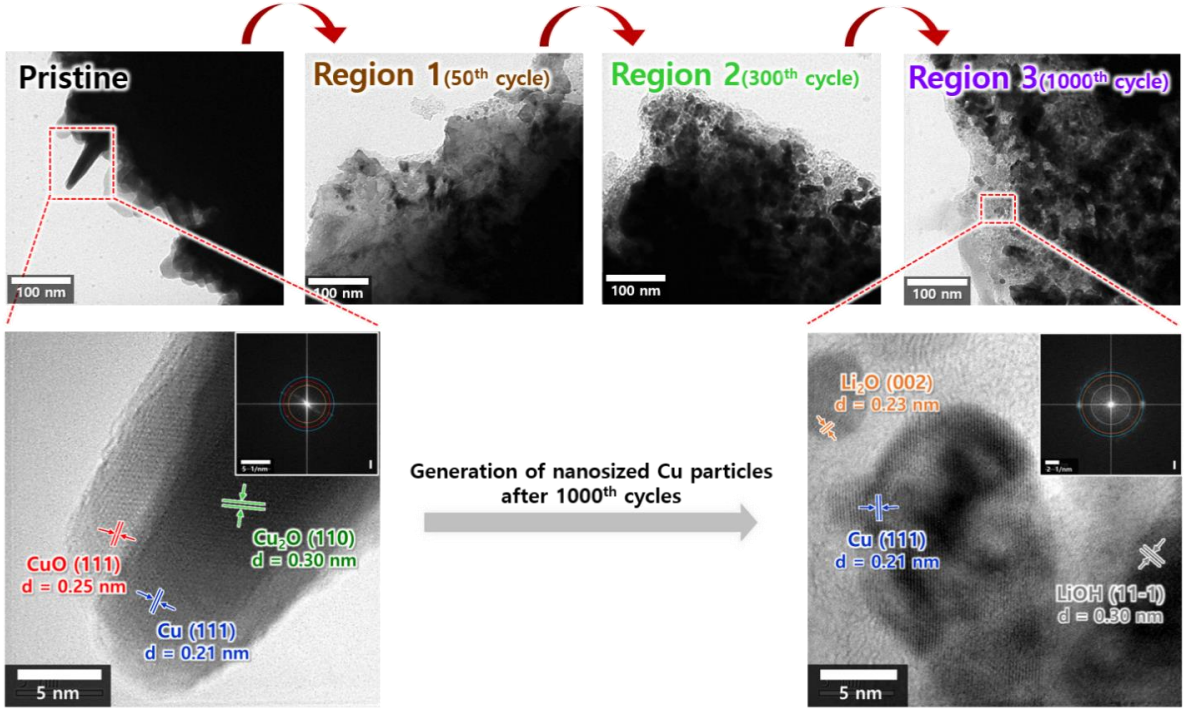

Fig. S14. HR-TEM images and SAED patterns (inset) of EP Cu-textile before (pristine) and after GCD cycling (50th, 300th, and 1000th cycle) in a fully discharged state. In this case, the Cu NPs formed by the continuous disintegration of copper oxides during lithiation process were clearly observed after Region 2 (300th cycle).

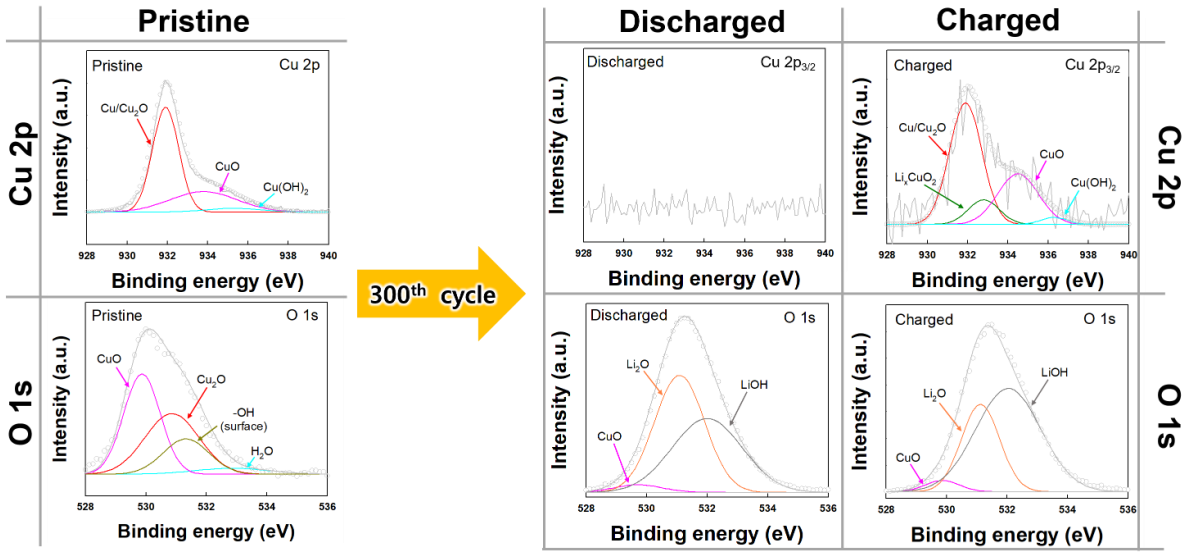

Fig. S15. *Ex situ* XPS spectra of EP Cu-textile at pristine state and Region 2 (after 300 cycles) corresponding to fully charged (3 V) and discharged (0.01 V) states. For Cu $2p_{3/2}$ XPS core peak at fully discharged state, no signal was observed due to the thickly formed SEI layer (≈15 nm) on the EP Cu-textile surface (the detectable depth of XPS is about 7nm), which could be confirmed by the deconvoluted O 1s spectrum indicating the formation of the SEI compounds. In this case, the O 1s spectrum had no signals for Cu_2O/CuO, indicating that the formed Cu_2O/CuO was reduced to metallic Cu. When the EP Cu-textile was fully charged to 3 V (delithiation), the deconvoluted Cu $2p_{3/2}$ peak showed an increased Cu_2O/CuO peak intensities, demonstrating that that the originated/converted metallic Cu was oxidized to Cu_2O/CuO.[S5]

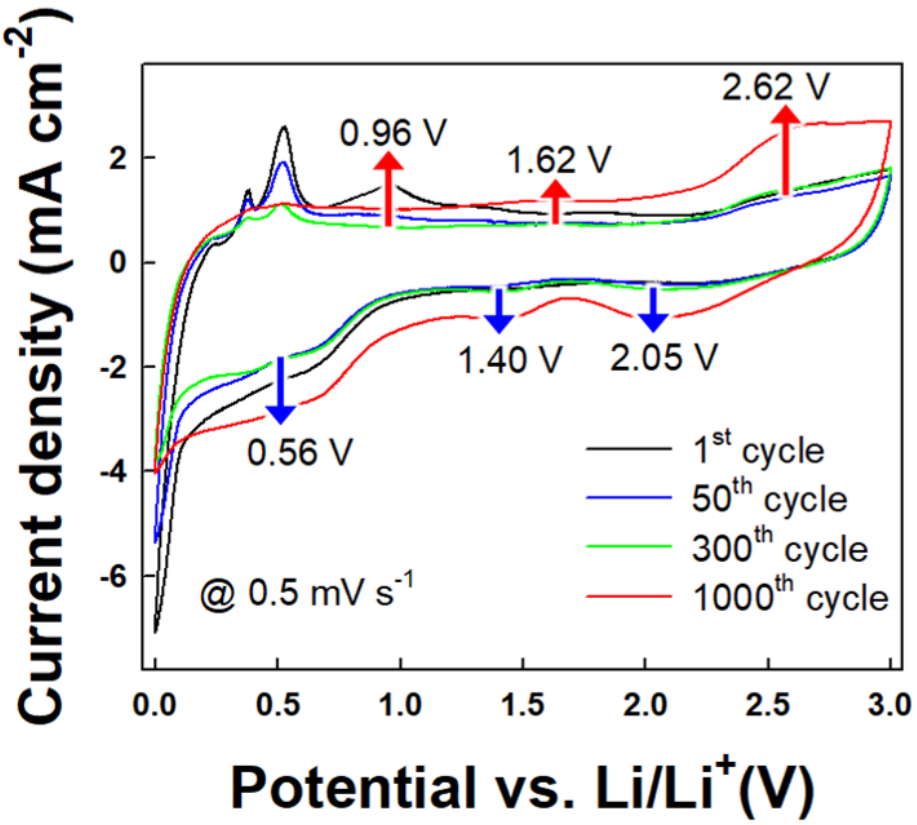

Fig. S16. CV curves of EP Cu-textile after 1st, 50th (Region 1), 300th (Region 2), and 1,000th (Region 3) GCD cycling, measured at a scan rate of 0.5 mV s^{-1} in the potential range of 0.01 – 3.0 V. The reduction peaks observed at around 2.05, 1.40 and 0.56 V corresponded to the formation of $Cu_{1-x}^{II}Cu_x^{I}O_{1-x/2}$ ($0 \leq x \leq 0.4$), Cu_2O, Cu and Li_2O, respectively. While the oxidation peaks at around 0.96, 1.62, and 2.62 V occurred from the decomposition of Li_2O and oxidations of Cu to Cu_2O and CuO, respectively.

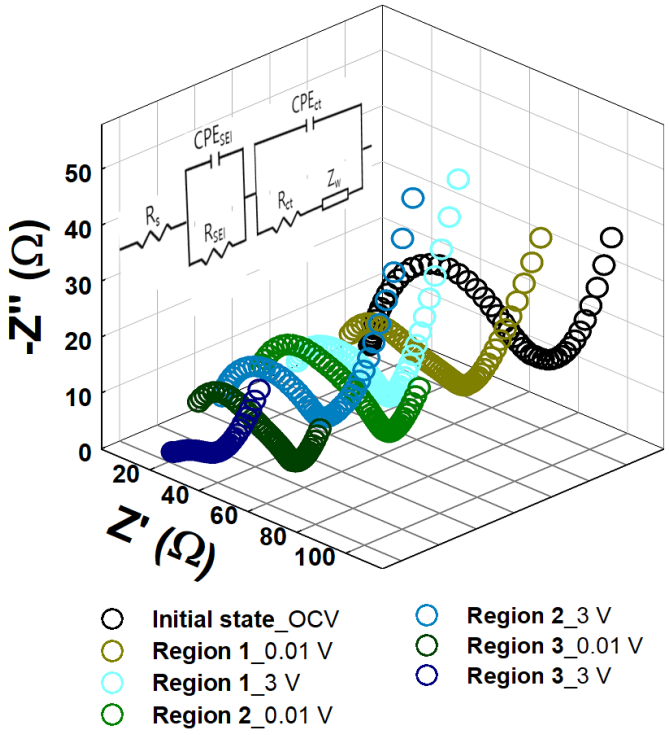

Potential vs. Li/Li⁺ (V)	R_s (Ω)	R_{SEI} (Ω)	R_{ct} (Ω)
Initial state (OCV)	9.4	-	55.9
Region 1 (Discharged state; 0.01 V)	11.3	21.4	25.8
Region 1 (Charged state; 3 V)	8.1	21.1	13.4
Region 2 (Discharged state; 0.01 V)	7.6	32.1	17.5
Region 2 (Charged state; 3 V)	9.1	7.2	26.5
Region 3 (Discharged state; 0.01 V)	11.5	21	20.3
Region 3 (Charged state; 3 V)	16.4	7.5	9.6

Fig. S17. The Nyquist curves of EP Cu-textile at initial and various charged (3 V)/discharged (0.01 V) states. All spectra obtained from the given charged/discharged states exhibited slightly depressed semicircles and slanted lines, and each component was analyzed based on the equivalent circuit shown in the inset. Herein, R_s, R_{SEI}, R_{ct}, and Z_w indicate electrolyte resistance, interface film (SEI layer) resistance, charge transfer resistance, and Warburg impedance, respectively. The values of each component shown in the table were obtained by applying CPE_{SEI} and CPE_{ct} instead of the ideal double-layer capacitance for the better fitting. The initial state of the EP Cu-textile electrode showed one clear semicircle at a high frequency region, corresponding to R_{ct}. On the other hand, the Nyquist curve of the discharged state (0.01 V) in Region 1 (~50th cycle) showed a depressed semicircle comprising R_{SEI} and R_{ct} components, indicating the initial formation of the SEI layer. When the electrode was fully charged to 3 V, the R_{SEI} value did not show a significant change, implying the electrochemical irreversibility of the SEI layer (i.e., incomplete SEI decomposition in the delithiation process). As the charge/discharge cycling of the EP Cu-textile electrode entered Region 2 (300th cycle), the R_{SEI} value, which had increased after discharging, decreased significantly when re-charging to 3 V, and this phenomenon was similarly observed in Region 3. These results suggest the reversible formation

(discharging step)/(partial) dissolution (charging step) of a catalytically generated polymeric gel-like film on the electrode surface (i.e., the outermost layer in contact with the electrolyte) during the electrochemical sweeps (i.e., Region 2 and 3). Importantly, such reversible formation/dissolution of the polymeric gel-like film can be accelerated by both the catalytic Cu NPs continuously generated during lithiation process and the newly formed flower-like 3D structure enabling larger active surface areas (see Fig. 3g), resulting in 'negative fading' of capacity. A slight increase in the R_s in Region 3 may be due to a local depletion of the electrolyte in the coin-type battery cell following a long-term GCD cycling involving formation/dissolution of the gel-like phase at the electrode/electrolyte interface. However, a noticeable decrease in the R_{ct} value in Region 3 indicated a more facile electrochemical reaction process, which was mainly attributed to the improved charge (ion/electron) transfer kinetics of the polymeric gel-like films as well as the formed 3D open structure.[S6]

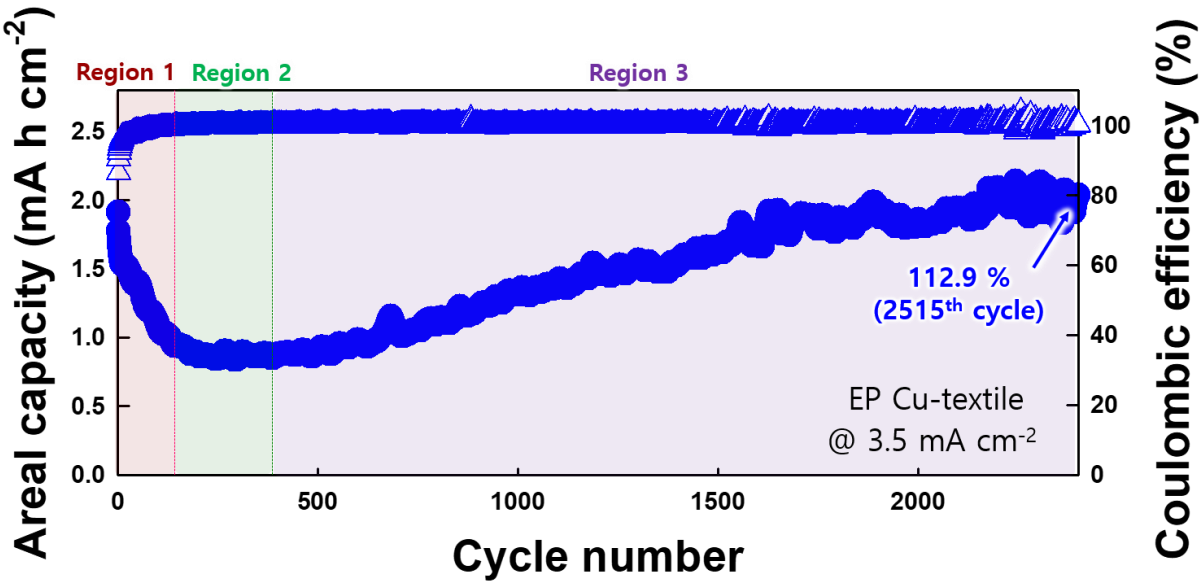

Fig. S18. Cycling stability of EP Cu-textile at a current density of 3.5 mA cm^{-2}.

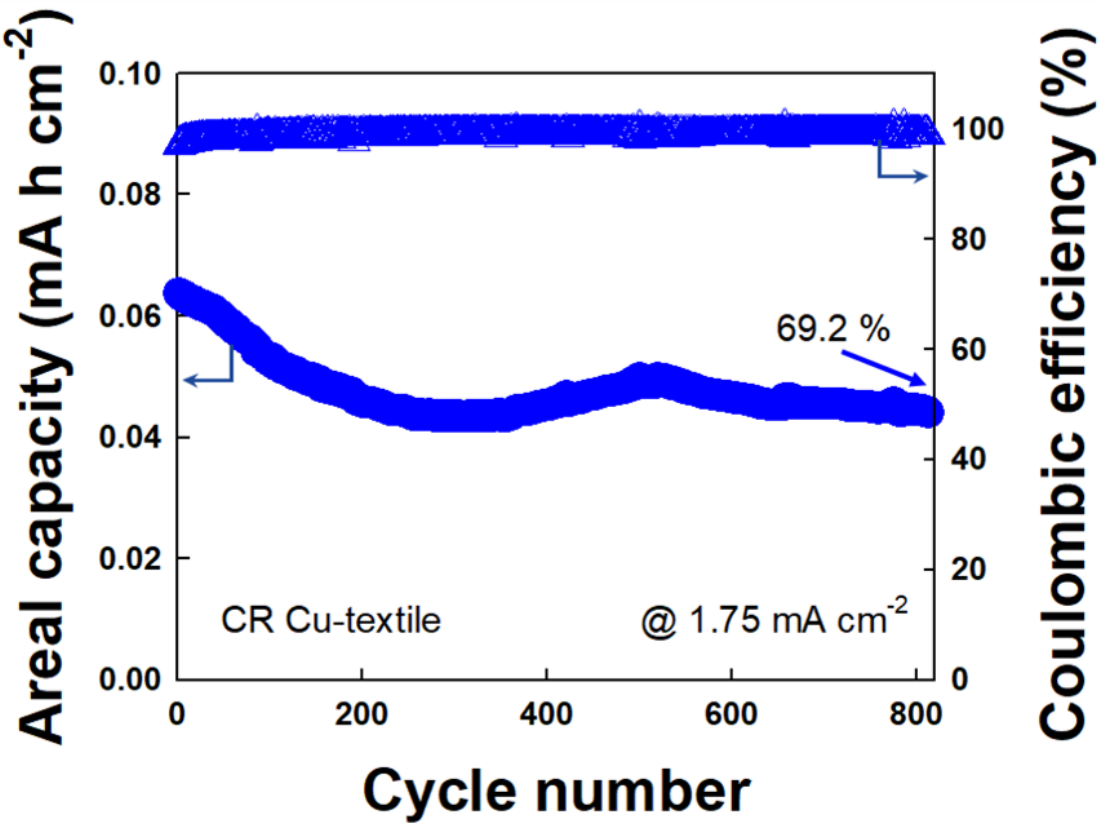

Fig. S19. Cycling stability of the CR Cu-textile at a current density of 1.75 mA cm^{-2}. An increase of areal capacity was observed after 300th cycle. However, after 500th cycle, unlike EP Cu-textile, the areal capacity of CR Cu-textile was decreased, again.

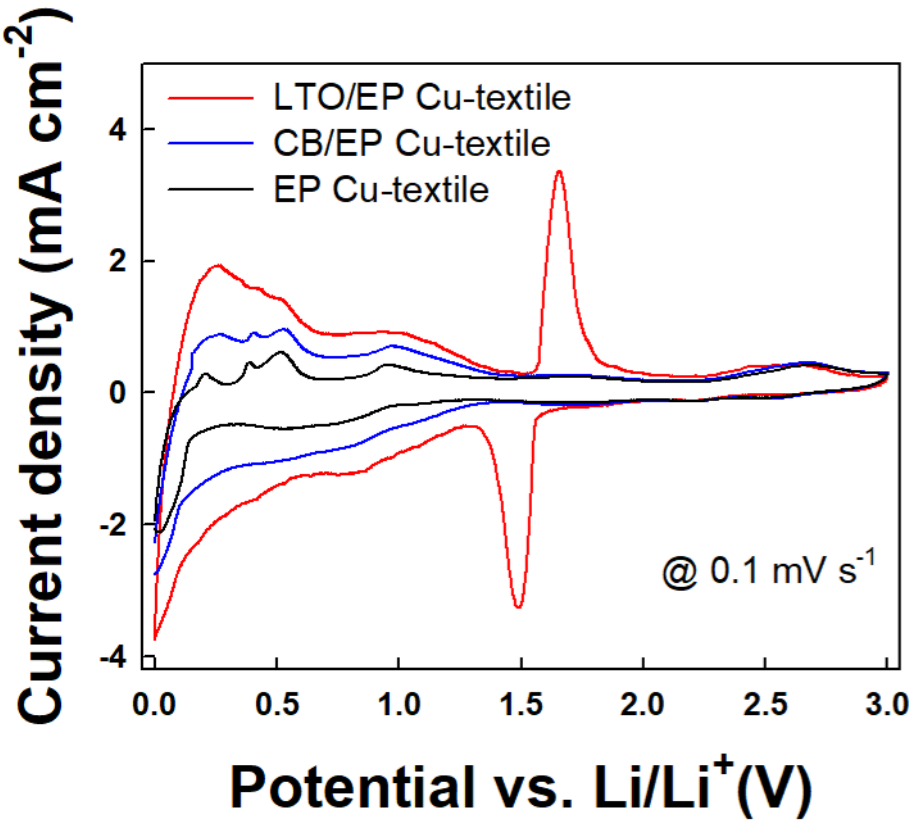

Fig. S20. CV curves of EP Cu-textile, CB/EP Cu-textile, and LTO/EP Cu-textile at a scan rate of 0.1 mV s^{-1}.

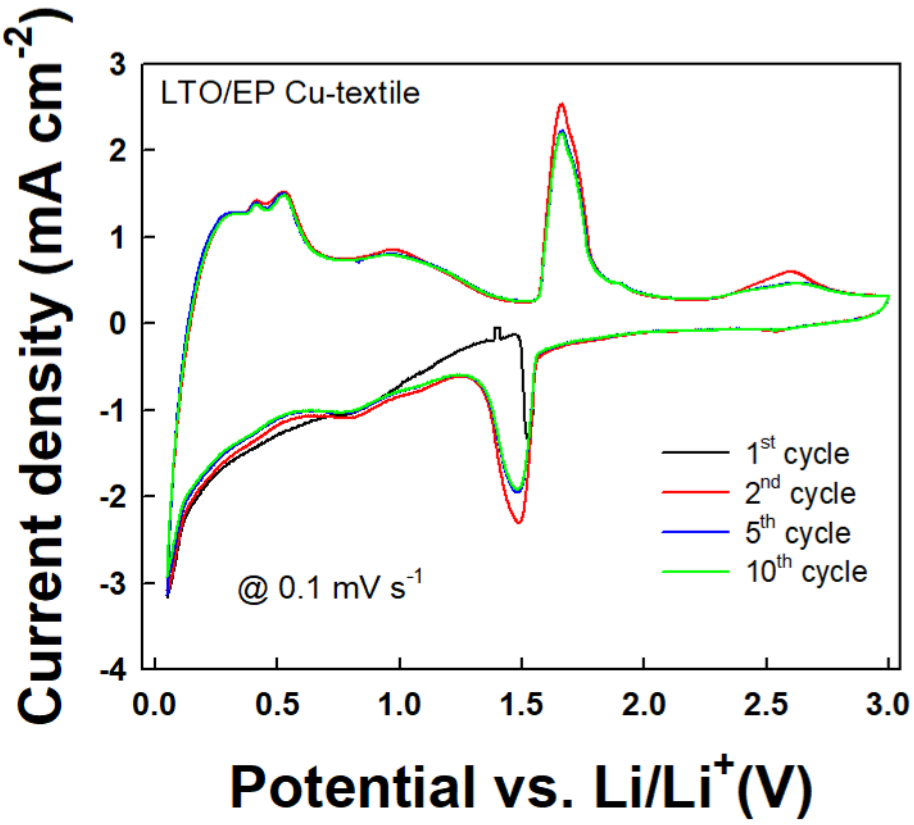

Fig. S21. CV curves of LTO/EP Cu-textile at a scan rate of 0.1 mV s^{-1}. The loading amount of LTO was adjusted to 10 mg cm^{-2}.

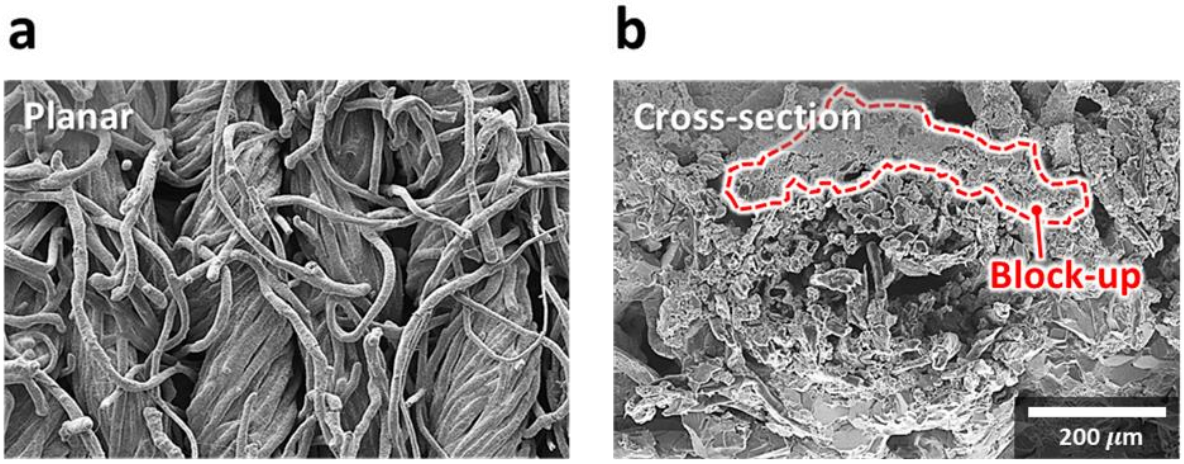

Fig. S22. (a) Planar and (b) cross-sectional FE-SEM images of MWCNT-textile after Cu electroplating. The Cu-plating on the 50-MWCNT-textiles without an Au NP layer displayed poor coating quality showing Cu agglomeration and blockage phenomena (**Fig. S22 (b)**). This is stark contrast with EP Cu-textile with Au NP layers shown in **Fig. 2e** in the manuscript.

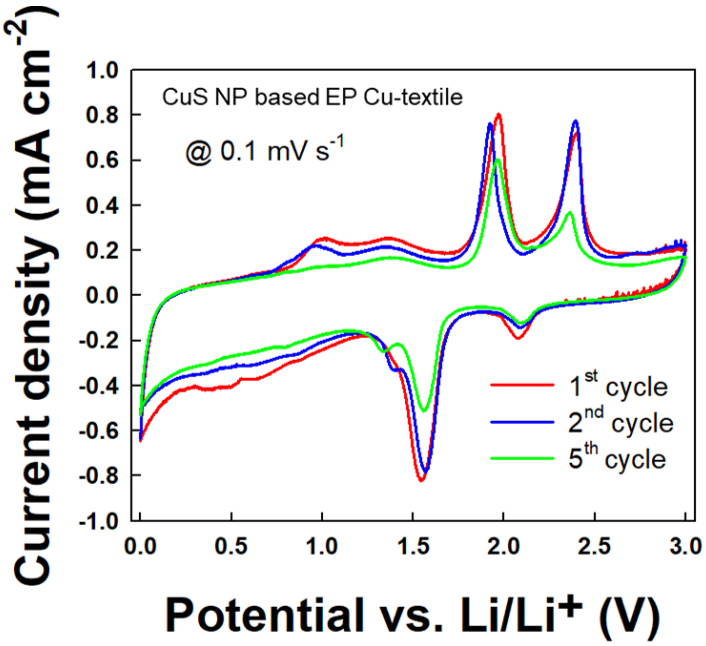

Fig. S23. CV curves at a scan rate of 0.1 mV s^{-1} for EP Cu-textiles prepared using CuS NP-based seed layers. In this case, the three reduction peaks at 2.27, 1.31, and near 0.72 V indicate the formation of a $Cu_{1-x}^{II}Cu_x^{I}O_{1-x/2}$ ($0 \leq x \leq 0.4$) solid solution, Cu_2O (from CuO), and the decomposition into Cu/Li_2O (from CuO), respectively. Additionally, the peaks at 2.06 and 1.52 V are attributed to the transformation from CuS to Li_xCuS and the conversion of Li_xCuS to Cu, respectively. Furthermore, the broad peaks at 1.48 and 2.55 V in the anodic sweeps were attributed to the oxidation of Cu to Cu_2O and CuO, respectively, while the two peaks detected at 1.94 and 2.36 V originated from the oxidation of Cu to CuS.

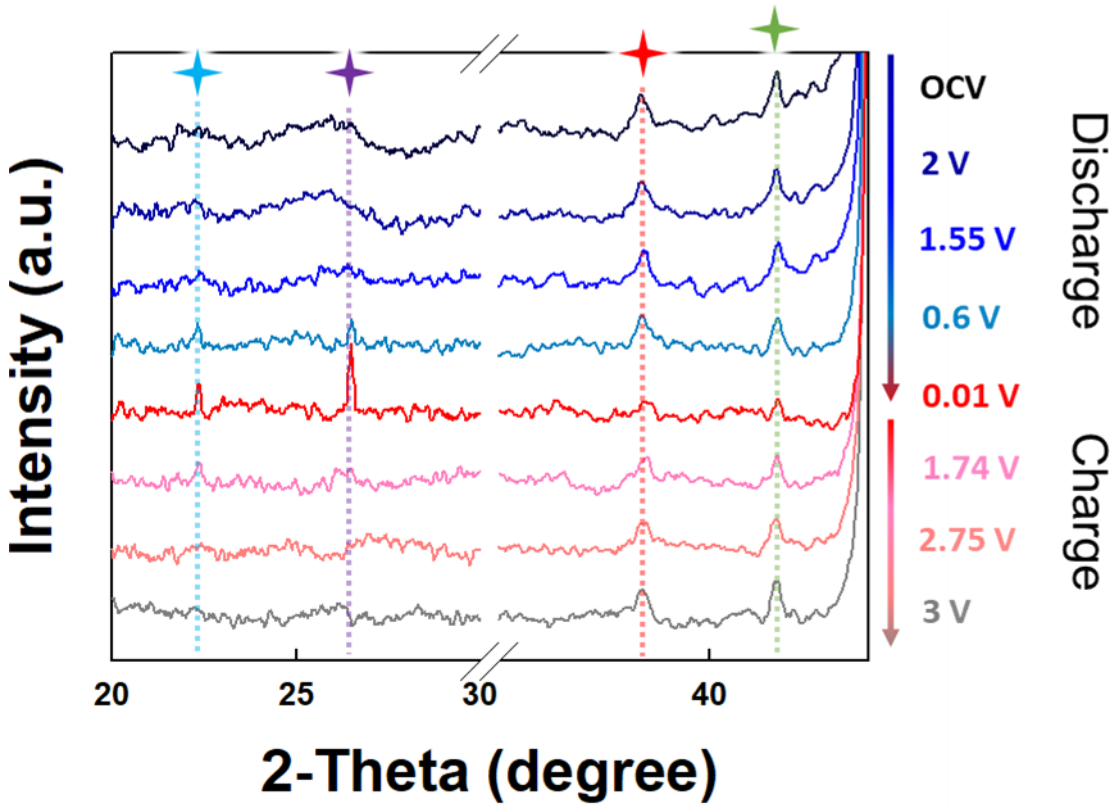

Fig. S24. *In situ* XRD patterns of EP Cu-textile recorded at different potentials during the initial GCD cycle (✦ - Li_2CO_3 (JCPDS file No. 80-1307), ✦ - LiOH(JCPDS file No. 85-0777), ✦ - CuO (JCPDS file No. 48-1548), ✦ - Cu_2O (JCPDS file No. 05-0667)). The EP Cu-textile at the open circuit voltage (OCV) state displayed strong peaks at 38.7°, 41.3°, and 46.8°, which corresponded to CuO (111), Cu_2O (200), and Cu (111), respectively. As the EP Cu-textile underwent the discharge state, new peaks for Li_2CO_3 and LiOH were appeared at 22.4° and 26.5°, suggesting the formation of the SEI layer. At the fully discharged state (0.01 V), the peak intensities of CuO and Cu_2O decreased, suggesting the partial reduction to the Cu phase with the formation of a thick SEI layer on the EP Cu-textile surface. When successively charging the EP Cu-textile to 3 V, the peak intensities of Li_2CO_3 and LiOH decreased, while the peaks for CuO and Cu_2O became stronger in comparison to the fully discharged state. The results indicate that the SEI layer is formed and dissolved reversibly with the phase transition of copper oxides during the successive discharge and charge processes.

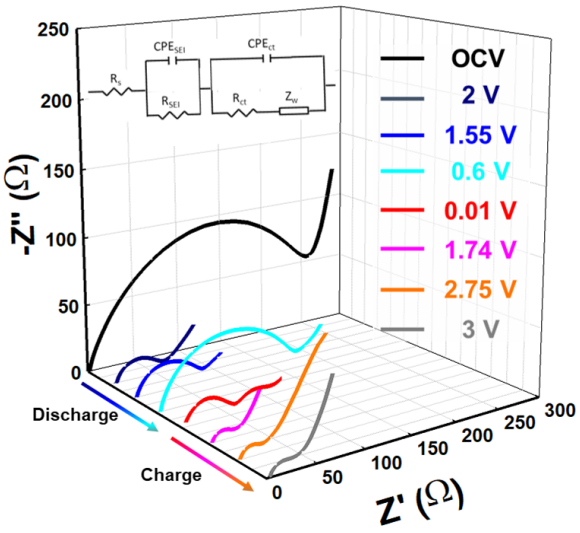

Potential vs. Li/Li⁺ (V)	R_s (Ω)	R_{ct} (Ω)	R_{SEI} (Ω)
OCV	1.873	249.7	-
2 V	3.76	16.93	6.23
1.55 V	4.493	28.88	34.88
0.6 V	4.046	44.81	84.14
0.01 V	4.157	49.43	51.8
1.74 V	3.566	4.77	13.31
2.75 V	3.144	13.04	2.32×10^{-5}
3 V	2.918	17.09	8.29×10^{-7}

Fig. S25. *In situ* EIS results of EP Cu-textile measured at different potentials during initial GCD cycle (right). The inset of the EIS data set shows a representative equivalent circuit for EP Cu-textile electrode, and each parameter is given in the Table (left). As the discharging proceeds, the SEI layer started to form and contribute to the R_{tot} of the electrode (i.e., R_{SEI}). The R_{tot} value at 2 V was significantly lower than that at the OCV state, possibly due to the presence of initially formed immature SEI layer with defects, gaps, and lithiophilic Li-compounds. These factors may facilitate ion transfer compared to the electrode at the OCV state. However, the R_{tot} rapidly increased from 27 to 133 Ω as the electrode discharged to 0.6 V due to the structural stress arising from phase transformation and the growth of the resistive SEI layer. At the fully discharged state (0.01 V), the R_{tot} slightly decreased to 104 Ω, due to the formation of a stable SEI layer and metallic Cu nanoparticles embedded in the Li_2O matrix. As the electrode charged to 2.75 V, R_{tot} linearly decreased (17 Ω) due to the decomposition of the reversible SEI layer, volume contraction, and delithiation. At the fully charged state (3 V), R_{tot} slightly increased due to the conversion of metallic Cu to CuO and Cu_2O states.

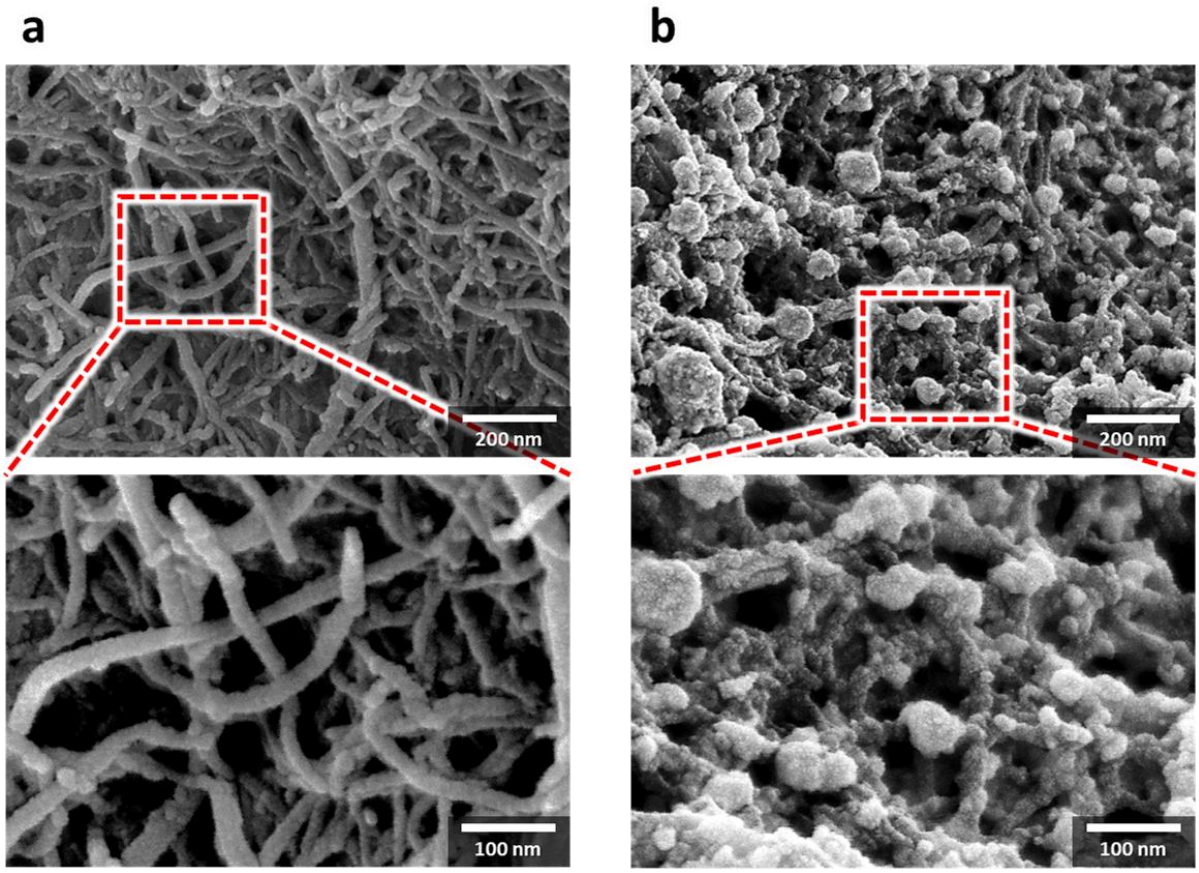

Fig. S26. FE-SEM images of (a) 5-MWCNT-textile and (b) Au NP-MWCNT-textile. The Au NPs were uniformly coated on all exposed surface of the 5-MWCNT-textile while maintaining the porous structure of the textiles was maintained. In this case, metallic fusion of adjacent Au NPs occurred and resulted in the formation of larger Au particles, suggesting that the small-molecule linker (TREN)-based LbL assembly significantly reduced the separation distance between each Au NPs.

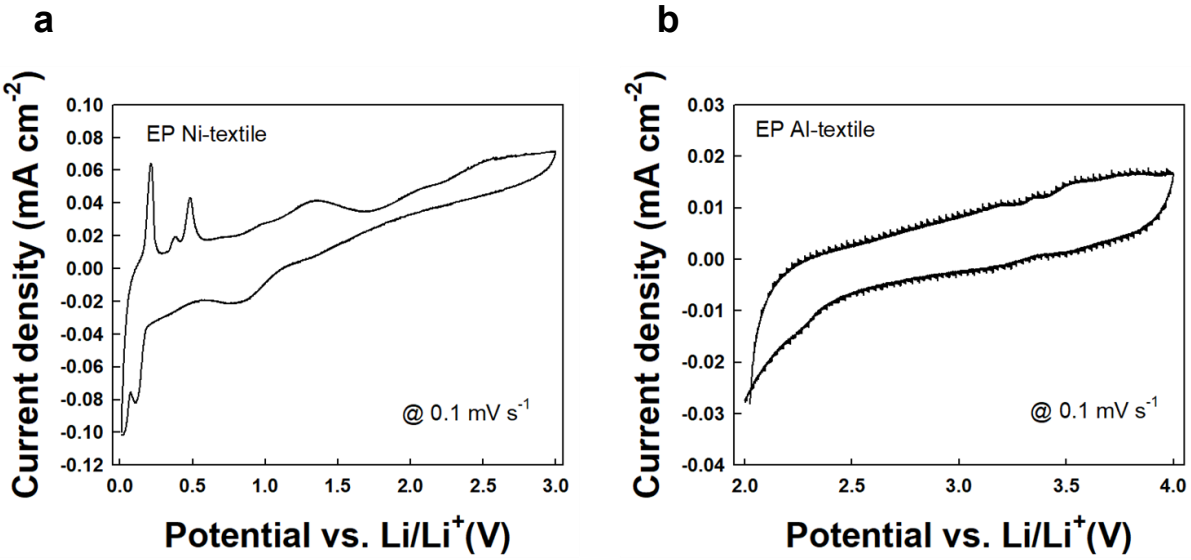

Fig. S27. 5th CVs for (a) EP Ni-textile and (b) EP Al-textile at a scan rate of 0.1 mV s^{-1}. The potential window for EP Ni-textile and EP Al-textile was adjusted to 0.01 – 3.0 V (vs. Li/Li^+) and 2.0 – 4.0 V (vs. Li/Li^+), respectively.

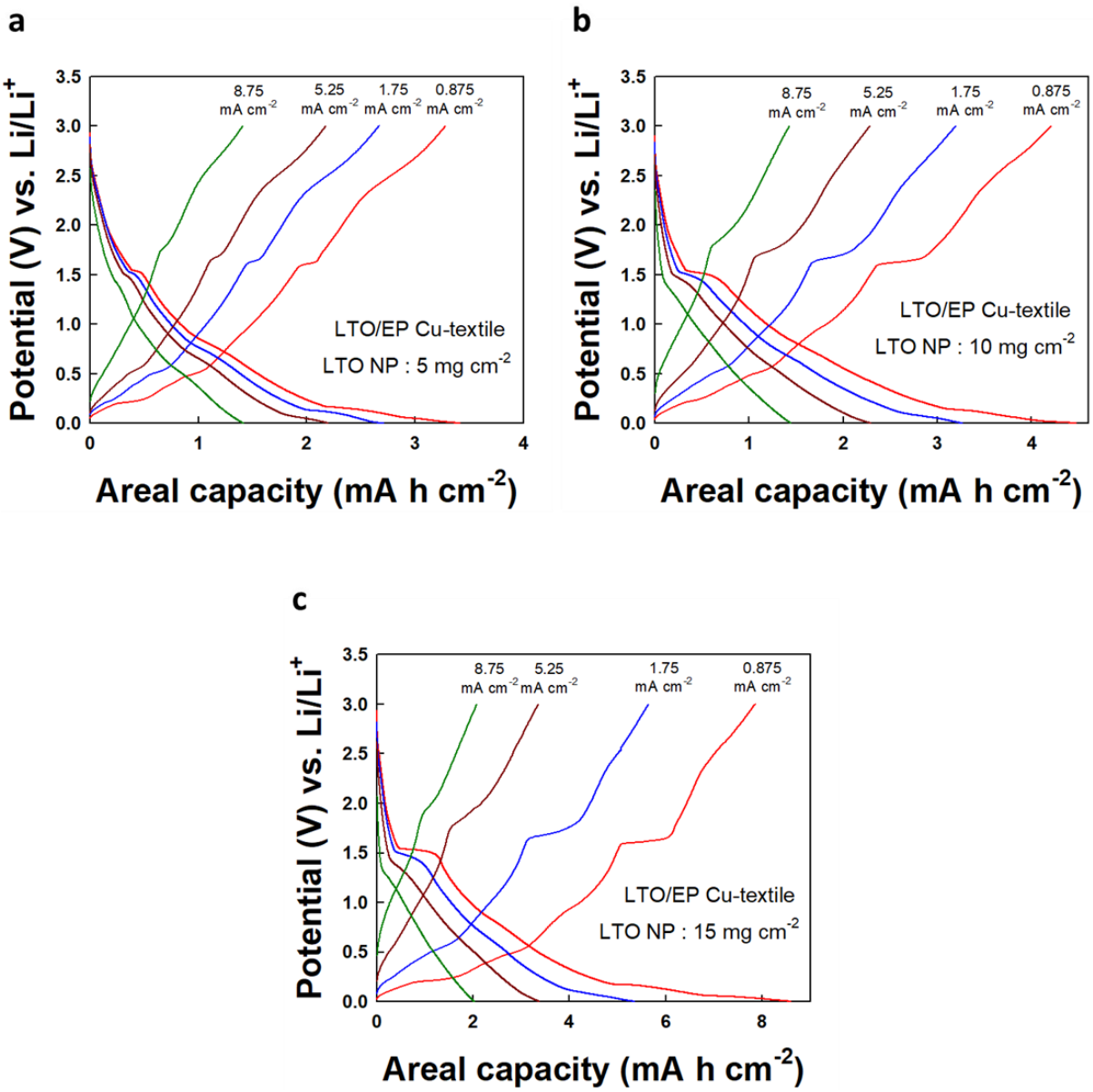

Fig. S28. GCD curves of LTO EP Cu-textile with different LTO loading of (a) 5, (b) 10, and (c) 15 mg cm^{-2} at various current densities of 0.875, 1.75, 8.25, and 8.75 mA cm^{-2}.

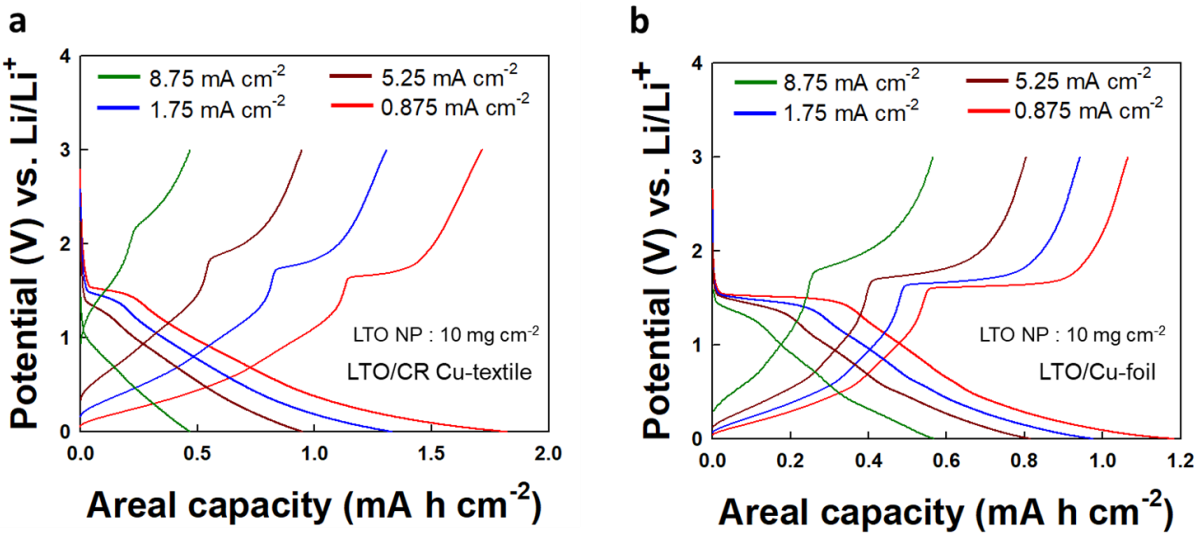

Fig. S29. GCD curves of (a) LTO/CR Cu-textile and (b) LTO/Cu-foil with 10 mg cm^{-2} LTO loading at various current densities.

Table S1. Comparison of areal capacities of CuO-based anodes.

Electrode materials	Substrate	Method	Mass loading (mg cm^{-2})	Areal capacity (mA h cm^{-2})	Cycle number	Ref.
CuO/Cu_2O	**EP Cu-textile**	**Electroplating and thermal oxidation**	**1.04**	**2.62 (at 1.75 mA cm^{-2})**	**~1,900**	**Our work**
CuO/Cu_2O	**EP Cu-textile**	**Electroplating and thermal oxidation**	**1.04**	**1.91 (at 3.5 mA cm^{-2})**	**~2,500**	**Our work**
Flower-like CuO/Cu_2O-CTAB	Copper mesh	Calcination, vulcanization, hydrothermal growth	-	1.1 (at 4 mA cm^{-2})	500	[S7]
CuO-Ge	Copper foam	Chemical treatment, radio frequency sputtering	0.67	3.45 (at 0.8 mA cm^{-2})	150	[S8]
C-doped CuO nanorods/CuO layer/Cu_2O layer	Carbon cloth	Magnetron sputtering, thermal oxidation	2.6	2.38	150	[S9]
CuO/CNT	Cotton Cloth	Electroless plating, in situ etching	1.1	0.8 (at 0.05 mA cm^{-2})	120	[S10]

CuO	Cu-Ni alloy foil	Chemical etching, post-thermal annealing	2.10	1.37 (at 0.15 C)	150	[S11]
CuO-MWCNT	Cu foil	Slurry coating	1.947	1.11 (at 0.39 mA cm^{-2})	400	[S12]

Table S2. Comparison of specific capacities of LTO-based anodes.

Electrode materials	Substrate	Method	Mass loading (mg cm^{-2})	Specific capacity (mA h g^{-1})	Ref.
LTO	**EP Cu-textile**	**Slurry coating**	**10**	**411 (at 0.5 C)**	**Our work**
LTO	Carbon fiber	Vacuum filtration	8.25	166 (at 0.1 C)	[S13]
LTO	Carbon cloth supported CNTs	Atomic layer deposition, lithiation	2	169 (at 1 C)	[S14]
LTO/rGO	Carbon fabric	Roll-pressed	-	155 (at 0.25 C)	[S15]
LTO	Copper-plated Paper	Slurry casting	0.22	125 (at 0.1 C)	[S16]

REFERENCES

[S1] A. J. Taylor, D. J. Graham, D. G. Castner, Analyst **140** (2015) 6005-6014.

[S2] Y. Wang, Y. L$\ddot{u}$, W. Zhan, Z. Xie, Q. Kuang, L. Zheng, J. Mater. Chem. A **3** (2015) 12796.

[S3] Y. Zhu, K. Mimura, S.-H. Hong, M. Isshiki, J. Electrochem. Soc. **152** (2005), B296-B301.

[S4] S. Y. Chew, S. H. Ng, J. Wang, P. Nov$\acute{a}$k, F. Krumeich, S. L. Chou, J. Chen, H. K. Liu, Carbon, **47** (2009) 2976-2983.

[S5] B. Gangaja, S. Chandrasekharan, S. Vadukumpully, S. V. Nair, D. Santhanagopalan, J. Power Sources, **340** (2017) 356-364.

[S6] S. Laruelle, S. Grugeon, P. Poizot, M. Doll$\acute{e}$, L. Dupont, J-M. Tarascon, J. Electrochem. Soc. **149** (2002) A627-A634.

[S7] X. Lei, Z. Liu, J. Ding, W. Cheng, Y. Guo, X. Tang, B. Wang, Y. Huang, Ceramics International 49 (2023) 2380-2387.

[S8] L. Deng, X. Li, H. Li, W. Cai, J. Wang, H. Zhang, H. Jia, X. Wang, S. Cheng, Front. Chem. 7 (2020) 869.

[S9] C. Tang, H. Zhang, D. Jiao, R. Hu, Z. Liu, Materials and Design 162 (2019) 52-59.

[S10] M. Shi, S. Wu, Z-D. Han, S. Li, Y-T. Pan, S. Yuan, Q. Wang, Rare Met. 40 (2021) 400-408.

[S11] J. Ha, Y-T. Kim, J. Choi, ChemSusChem 13 (2020) 419-425.

[S12] J. Xu, Y. Liu, L. He, C. Zhang, Y. Zhang, Ceramics International 42 (2016) 12027-12032.

[S13] H. Lu, J. Hagberg, G. Lindbergh, A. Cornell, Nano Energy 39 (2017) 140-150.

[S14] Z. Yao, X. Xia, C-a. Zhou, Y. Zhong, Y. Wang, S. Deng, W. Wang, X. Wang, J. Tu, Adv. Sci. 5 (2018) 1700786.

[S15] S. H. Ha, K. H. Shin, H. W. Park, Y. J. Lee, Small 14 (2018) 1703418.

[S16] Z. Wang, A. Malti, L. Ouyang, D. Tu, W. Tian, L. Wågberg, M. M. Hamedi, Small 14 (2018) 1803313.